Texture Development in a Friction Stir Lap-Welded AZ31B Magnesium Alloy

B.S. NAIK, D.L. CHEN, X. CAO, and P. WANJARA

The present study was aimed at characterizing the microstructure, texture, hardness, and tensile properties of an AZ31B-H24 Mg alloy that was friction stir lap welded (FSLWed) at varying tool rotational rates and welding speeds. Friction stir lap welding (FSLW) resulted in the presence of recrystallized grains and an associated hardness drop in the stir zone (SZ). Microstructural investigation showed that both the AZ31B-H24 Mg base metal (BM) and SZ contained β-$Mg_{17}Al_{12}$ and Al_8Mn_5 second phase particles. The AZ31B-H24 BM contained a type of basal texture $(0001)\langle 11\bar{2}0 \rangle$ with the (0001) plane nearly parallel to the rolled sheet surface and $\langle 11\bar{2}0 \rangle$ directions aligned in the rolling direction. FSLW resulted in the formation of another type of basal texture $(0001)\langle 10\bar{1}0 \rangle$ in the SZ, where the basal planes (0001) became slightly tilted toward the transverse direction, and the prismatic planes $(10\bar{1}0)$ and pyramidal planes $(10\bar{1}1)$ exhibited a 30 deg $+ (n - 1) \times 60$ deg rotation ($n = 1, 2, 3, \ldots$) with respect to the rolled sheet normal direction, due to the shear plastic flow near the pin surface that occurred from the intense local stirring. With increasing tool rotational rate and decreasing welding speed, the maximum intensity of the basal poles (0001) in the SZ decreased due to a higher degree of dynamic recrystallization that led to a weaker or more random texture. The tool rotational rate and welding speed had a strong effect on the failure load of FSLWed joints. A combination of relatively high welding speed (20 mm/s) and low tool rotational rate (1000 rpm) was observed to be capable of achieving a high failure load. This was attributed to the relatively small recrystallized grains and high intensity of the basal poles in the SZ arising from the low heat input as well as the presence of a small hooking defect.

I. INTRODUCTION

THE considerable challenges facing the transportation industry are rooted to the increasing concerns about global climate change in conjunction with highly volatile and rising energy prices.[1–6] With the understanding that roughly 85 pct of the anthropogenic environment-damaging emissions generated by aircraft and ground vehicles occur from their useful life, it is unsurprising that lightweight design has become a key strategy by which the transportation sector can address the greater world-wide societal demands for environmental and ecological stewardship and consumer demands for improved fuel efficiency and economy.[7–10] With due consideration of different lightweight materials (*e.g.*, aluminum alloys, advanced high strength steels, magnesium alloys, titanium alloys, and composites) for next-generation transportation aircraft and vehicles in the aerospace, automotive and rail industries, magnesium alloys offer a good combination of properties including low density, high strength-to-weight ratio, environmental friendliness, castability, and recyclability.[1,11–17] However, due to the limited number of slip systems in the hexagonal close-packed (hcp) crystal structure, magnesium alloys may be restricted in their widespread use by their poor ductility at room temperature. To diversify and expand the use of magnesium alloys in the transportation sector, enabling joining technologies are enviable for realizing cost-effective manufacturing and high performance assemblies.

Several joining technologies have shown potential for assembly of magnesium alloys including conventional arc and advanced fusion (*e.g.*, laser and electron beam) welding as well as friction stir welding (FSW). As the solidification defects and structure (*e.g.*, dendritic, coarse grains) in the fusion zone of welded magnesium alloys limit the mechanical performance, the realization of a solid-state joint using FSW is especially propitious for mitigating the formation of gas porosity, reducing the susceptibility to solidification cracking, limiting the compositional segregation of alloying elements and promoting/maintaining a wrought microstructure in the weldment. Moreover, the low heat input and process flexibility of FSW enable assembly of different joint configurations (*e.g.*, lap-, butt-, and T-joints) and

B.S. NAIK, Ph.D. Student, and D.L. CHEN, Professor and Ryerson Research Chair, are with the Department of Mechanical and Industrial Engineering, Ryerson University, 350 Victoria Street, Toronto, ON M5B 2K3, Canada. Contact e-mail: dchen@ryerson.ca X.CAO, Adjunct Professor, is with the Department of Mechanical and Industrial Engineering, Ryerson University, and also Senior Research Officer with the National Research Council Canada - Aerospace, 5145 Decelles Avenue, Montreal, QC H3T 2B2, Canada. P. WANJARA, Group Leader, is with the National Research Council Canada - Aerospace.

material forms (*e.g.*, cast, extruded, and rolled products) without requiring complicated surface preparation or shielding gas protection.[17–19]

Considering the potential of the FSW process for assembly of magnesium alloys, several studies have been conducted to investigate the inter-relationship between the parametric conditions, microstructure and mechanical properties for butt[17,20–24] and lap joints.[16,25,26] Recently, the investigation of the crystallographic orientations stemming from the FSW process is also becoming an avid area of research interest[16,20,27–29] to understand the influence of the severe plastic deformation occurring at elevated temperatures on the texture evolution in the SZ and thermomechanically affected zones (TMAZ)[30,31] of the welds. Besides understanding the changes in the basal, prismatic, and pyramidal planes during FSW of AZ31B-H24 Mg alloy, the correlation of the texture evolution to the mechanical performance of the welded assembly must be characterized. To the best of our knowledge, however, the texture changes from the FSW process and their resulting influence on the properties for Mg alloy lap welds have not been reported to date. The present investigation was, therefore, aimed at evaluating the effect of tool rotational rate and welding speed on the microstructure, texture and mechanical properties of a friction stir lap-welded (FSLWed) AZ31B-H24 Mg alloy. As part of the microstructural analysis, the texture of the FSLWed AZ31B-H24 Mg alloy sheets was studied by pole figure measurements, and the crystallographic orientations of the basal, prismatic, and pyramidal planes are discussed.

II. EXPERIMENTAL PROCEDURE

The material used in the present study was AZ31B-H24 Mg alloy in sheet form with a thickness of 2 mm and dimensions of 1200 mm × 500 mm. The nominal chemical composition of the AZ31B-H24 Mg alloy was 2.5 to 3.5 wt pct Al, 0.7 to 1.3 wt pct Zn, 0.2 to 1.0 wt pct Mn, and the balance Mg. Coupons of 300 mm (length) × 100 mm (width) were sectioned from the as-received sheets. Surface preparation of the sheets prior to friction stir lap welding (FSLW) consisted of cleaning the faying surfaces and the surrounding areas with ethanol, followed by scouring with an abrasive pad to remove the oxides and final cleaning in ethanol. The sheets were then overlapped with a width of approximately 28 mm, as indicated in Figure 1(a) and (b), and tightly clamped using spacers within a welding fixture that was secured to the backing anvil/worktable of an ISTIR MTS FSW machine. FSLW was carried out in position control mode using a H13 steel tool (46.6 to 50 HRC) that consisted of a scrolled shoulder with a diameter of 19.05 mm and an adjustable ¼-20 left-hand threaded pin having a diameter of 6.35 mm, a thread length of 4.45 mm, a thread spacing of 1.27 mm, and a pitch of 0.8 thread/mm. The angle between the tool and top sheet was maintained at 0.5 deg with a shoulder heel plunge depth (the portion of the shoulder under the surface of the top sheet) of approximately 0.25 mm in all the welding experiments. The welding direction (WD) was perpendicular to the rolling direction (RD) of the work-piece (Figure 1(c)). All the joints were FSLWed at a welding speed of 10 or 20 mm/s, a tool rotational rate of 1000 and 1500 rpm, and a pin length of 2.75 mm. It is noteworthy that relative to the welding and tool rotational directions indicated in Figure 1, the welds were manufactured with the retreating side (RS) near the edge of the top sheet, abbreviated as RNE.

The weld integrity was characterized in terms of the microstructure, texture, hardness, and lap tensile shear properties. For each FSLWed assembly, the unstable (ramp up and ramp down) regions at the beginning (~50 mm) and end (~20 mm) of the weld were removed. Using a precision abrasive waterjet cutting machine, the FSLWed assemblies were sectioned in the direction perpendicular to the WD to examine the microstructures in the weld cross-sections. The sectioned coupons were then cold mounted, ground, polished, and etched with a solution of acetic picral [10 mL acetic acid (99 pct), 4.2 g picric acid, 10 mL H_2O, and 70 mL ethanol (95 pct)] for approximately 6 seconds to reveal the grain structure. Microstructural analysis was carried out using an optical microscope equipped with quantitative image analysis software. The microhardness profiles were measured across the lap-welded samples (with a polished surface finish) at a load of 100 g and a dwell time of 15 seconds using an automated Buehler Vickers microindentation machine that was calibrated using a standard reference test block prior to testing. For each weld condition, the hardness profiles across the lap welds were obtained at mid-thickness of the top and bottom sheets with an indent interval of 0.3 mm (*i.e.*, at least three times the diagonal length of the indentation so as to prevent any potential effect of strain fields caused by adjacent indentations).

X-ray diffraction (XRD) patterns were determined using CuK_α radiation at 45 kV and 40 mA. The diffraction angle (2θ) at which the X-rays encroached on the sample varied from 20 deg to 90 deg with a step size of 0.05 deg and 3 seconds in each step. The crystallographic texture distribution of the FSLWed specimens was measured by a PanalyticalX'Pert PRO X-ray diffractometer (XRD) using CuK_α radiation (wavelength $\lambda = 0.15406$ nm) at 45 kV and 40 mA with a sample tilt angle ranging from 0 deg to 70 deg. The samples on the XRD sample stage were mounted in such a way that the RD of the sheet was oriented parallel to the X-axis of the sample stage, with the X-ray incident beam being impinged on the top surface of the lap welds. Figure 1(c) shows the positions that correspond to the texture measurements evaluated in different regions of the weldment (*i.e.*, BM, HAZ, TMAZ, and SZ) from the top surface of the sample, where the heat-affected zone (HAZ) and TMAZ occurred at 9.5 and 4.5 mm, respectively, from the center of the SZ on the advancing side (AS), while the BM was located at 50 mm from the center of the SZ on the AS. However, due to the relatively large measurement volume of the XRD technique, some potential overlaps may exist for each exposed area at a given location, which could slightly influence the pole figure intensity. The pole figures were then analyzed by the MTEX software,[32] where the results were represented as (0001), (10$\bar{1}$0), and (10$\bar{1}$1) color-scale intensity poles with
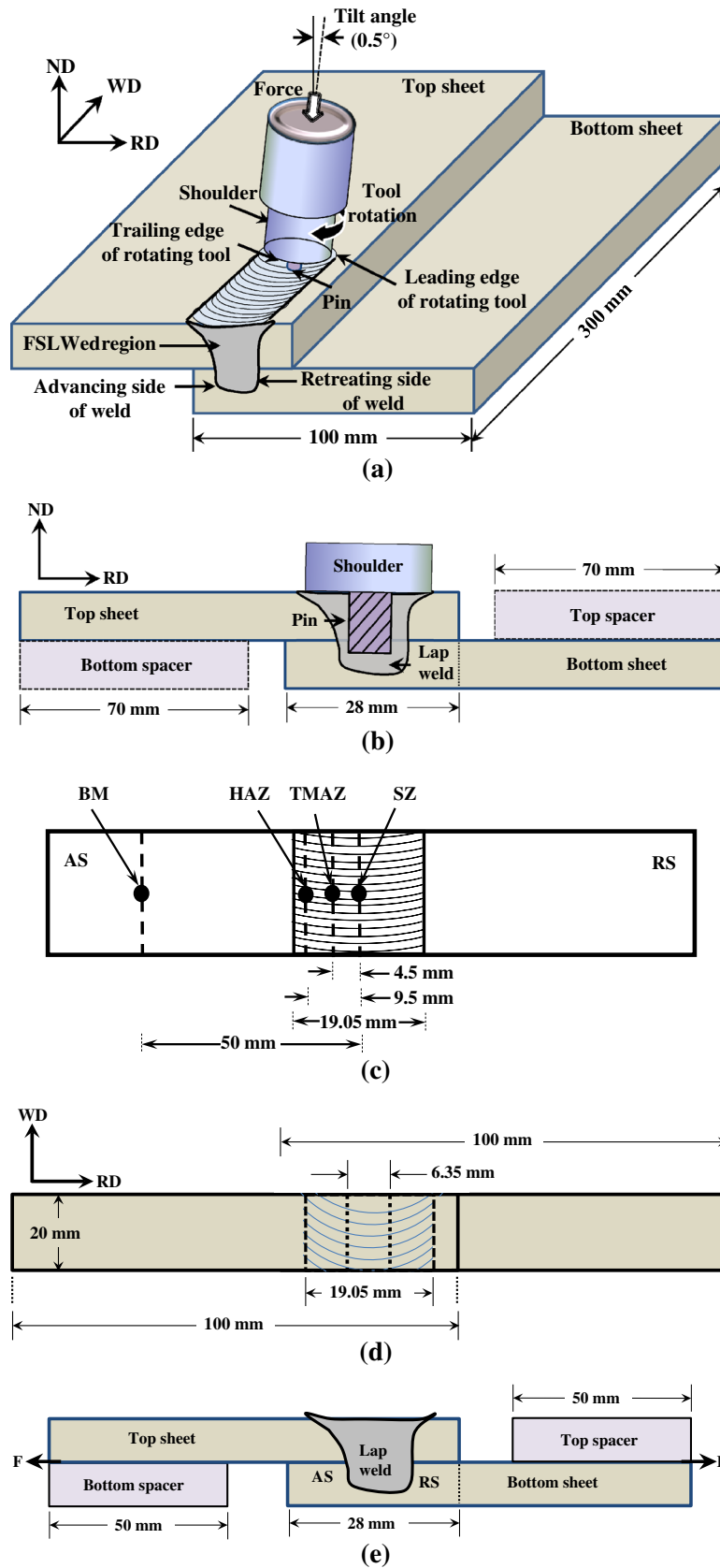
Fig. 1—Schematic diagrams of the experimental setup showing (*a*) the FSLW process, (*b*) the side view of the overlapped Mg/Mg joint, (*c*) the top view of the welded sample showing the corresponding locations for the pole figure measurements, (*d*) the top view of the tensile lap shear testing coupon, and (*e*) the setup for tensile/shear testing.
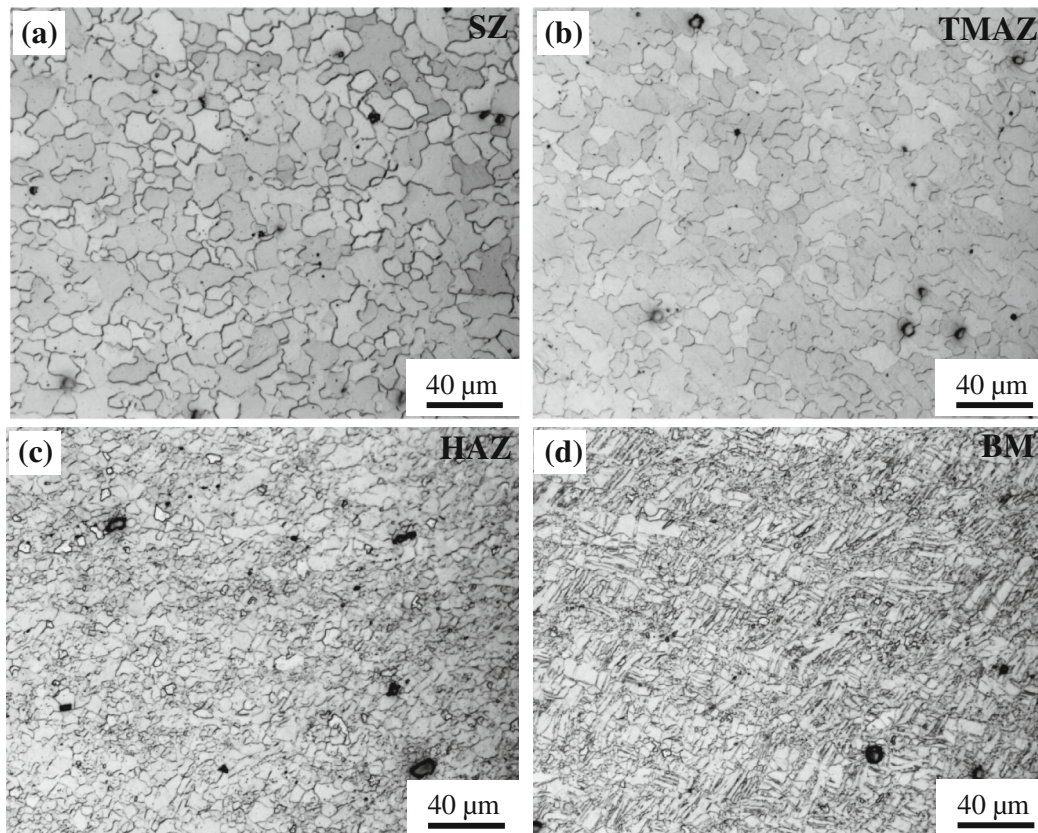
Fig. 2—Typical microstructures of the FSLWed AZ31B-H24 Mg alloy at a tool rotational rate of 1000 rpm and a welding speed of 20 mm/s in (*a*) SZ, (*b*) TMAZ, (*c*) HAZ, and (*d*) BM.

the vertical direction as the RD. Defocusing due to the rotation of sample holder was corrected using experimentally determined data from the diffraction of magnesium powders.

For each welded assembly, lap tensile shear specimens with a width of 20 mm and an overall length of approximately 160 mm (Figure 1(c)), according to ASTM D3164,[33] were also cut using a precision abrasive waterjet cutting system. Tensile shear tests were performed at room temperature using a fully computerized United tensile testing machine at a crosshead speed of 1 mm/min for each weld condition. To balance the offset axes of the lap members and minimize bending effects, two spacers having the same thickness as the sheet (*i.e.*, 2 mm) were used during the lap tensile shear tests, as illustrated in Figure 1(d). Fracture surfaces of the FSLWed joints after tensile shear testing were examined using a JEOL6380LV scanning electron microscope (SEM) equipped with an Oxford energy dispersive X-ray spectroscopy (EDS) and a three-dimensional fractographic imaging and analysis tool.

III. RESULTS AND DISCUSSION

A. *Microstructure*

Based on the microstructural characterization, three distinct zones, namely the SZ, TMAZ and HAZ, could

be identified in the friction stir lap welds of the AZ31B-H24 Mg alloy. The typical microstructures of the three zones are shown in Figures 2, 3, and 4 for tool rotational rates of 1000 and 1500 rpm at a welding speed of 20 and 10 mm/s, respectively. It is clear that the SZ, TMAZ, and HAZ exhibited different grain structural features, which were attributed to the difference in the frictional heat and material flow characteristics caused by the FSW process. The as-received microstructure of the BM consisted of fine recrystallized equiaxed grains and elongated/deformed pancake-like grains, as shown in Figures 2(d), 3(d), and 4(d). The heterogeneous grain structure and size in the BM originated from the incomplete dynamic recrystallization (partial annealing) during the warm rolling process as noted in Reference 25. The severe plastic deformation (from the mechanical stirring) and high temperature (from the frictional heating) during FSLW led to near-complete dynamic recrystallization as evidenced by the equiaxed morphology for all the grains in the SZ (Figures 2(a), 3(a), 4(a)) and TMAZ (Figures 2(b), 3(b), 4(b)). However, the simultaneous increase in the average grain size of the SZ and TMAZ (Table I) relative to the BM suggests the occurrence of both recrystallization and grain coarsening under the welding conditions applied in this study. The HAZ microstructure (Figures 2(c), 3(c), and 4(c)) was more similar to that of the BM but with a greater fraction of equiaxed grains and a slightly coarser grain size (Table I). This was attributed to the
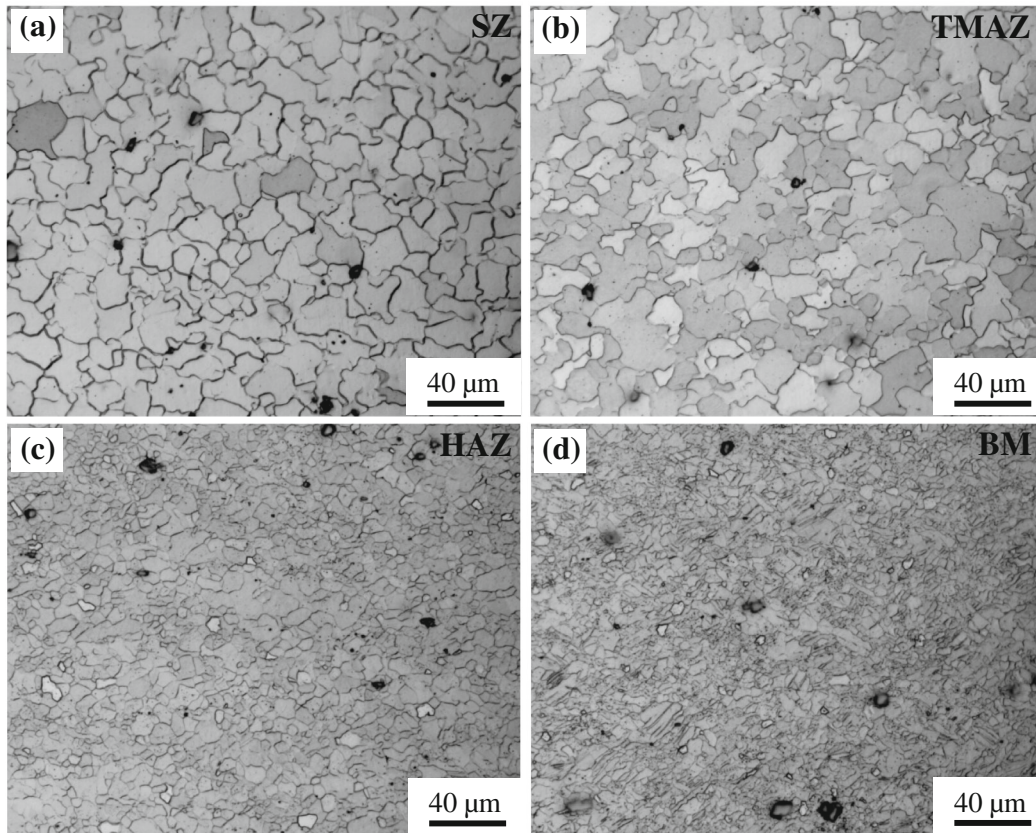
Fig. 3—Typical microstructures of the FSLWed AZ31B-H24 Mg alloy at a tool rotational rate of 1500 rpm and a welding speed of 20 mm/s in (a) SZ, (b) TMAZ, (c) HAZ, and (d) BM.

dominating effect of frictional heating that caused partial recrystallization of some elongated/deformed grains and the coarsening of the recrystallized grains. The microstructural evolution observed in the different regions of the FSLWed AZ31B-H24 Mg alloy was consistent with that which occurred in the friction stir butt welds of the AZ31B-H24 Mg alloy.[20–23,34,35]

Comparing Figures 2 with 3, it is apparent that grain coarsening occurred in the SZ with increasing tool rotational rate at a constant welding speed of 20 mm/s. Similarly, decreasing the welding speed at a fixed tool rotational rate of 1500 rpm was observed to result in grain coarsening, as illustrated in Figures 3 and 4 and tabulated in Table I. The grain coarsening is attributed to the increasing heat input during FSW that can be deliberated through the weld pitch (defined as a ratio of the welding speed to the tool rotational rate). Specifically, a low weld pitch value (0.4 mm/revolution) for the 1500 rpm and 10 mm/s, which indicates a "hot" welding condition, would render a coarse grain structure relative to the higher weld pitch value (0.8 mm/revolution and 1.2 mm/revolution) or "colder" welding conditions at 1500 rpm, 20 mm/s and 1000 rpm, 20 mm/s.

SEM examinations of the BM microstructure revealed a relatively homogeneous α-Mg matrix and the presence of relatively fine (~30 μm^2) particles, as indicated by arrows in Figure 5(a). EDS analysis (Figure 5(c)) indicated that these particles were on

average 61.4 at. pct Al and 38.6 at. pct Mn (Table II). Taking into consideration the binary phase diagram of Al-Mn,[36] these particles are likely to be Al_8Mn_5, which has a Mn content between 37 and 50 at. pct. In the SZ, two types of particles were present (Table II). Specifically, the slightly larger particles in the SZ (Figure 5(b)) were identified as Al_8Mn_5 based on the EDS analysis. The finer (~15 μm^2) particles (Figure 5(b)) were, on average, approximately 34.4 at. pct Al and 55.9 at. pct Mg (Table II; Figure 5(d)) and appeared to correspond to the β-$Mg_{17}Al_{12}$, based on the Al-Mg binary phase diagram.[37]

The nature of the intermetallic phases present in the BM and SZ was also investigated by XRD. Figure 6 shows the results of the XRD analysis for the BM and SZ in the samples assembled with different tool rotational rates and welding speeds. Specifically for the BM prior to FSW, the XRD analysis revealed distinct peaks of the Al_8Mn_5 and β-$Mg_{17}Al_{12}$ phases, along with some peaks that overlapped with the Mg peaks, as illustrated in Figure 6(a). XRD characterization of the FSLWed joint (Figures 6(b) through (d)) also showed independent peaks for the Al_8Mn_5 and β-$Mg_{17}Al_{12}$ phases, along with some peaks that coincided with Mg. It is noteworthy that intermetallic phases, such as β-$Mg_{17}Al_{12}$ particles, when present in AZ31B-H24 Mg alloy, are known to be brittle[38]; however, these β-$Mg_{17}Al_{12}$ particles are also present in the BM, so
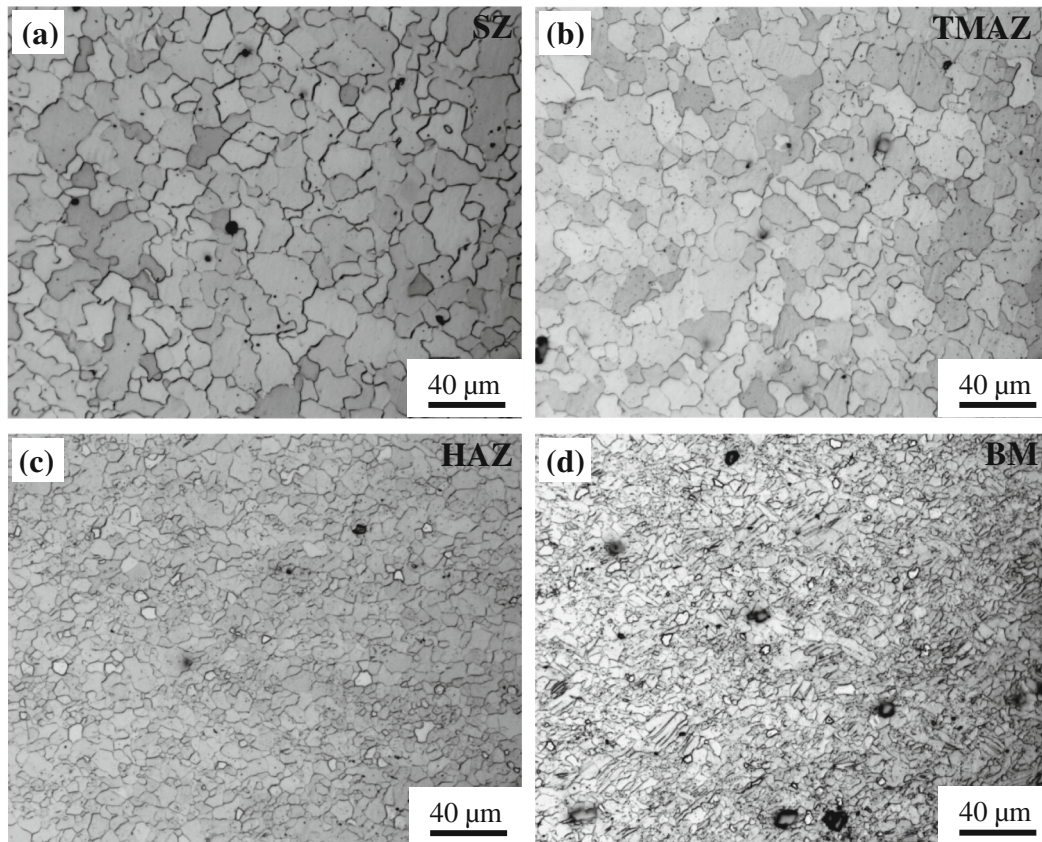
Fig. 4—Typical microstructures of the FSLWed AZ31B-H24 Mg alloy at a tool rotational rate of 1500 rpm and a welding speed of 10 mm/s in (*a*) SZ, (*b*) TMAZ, (*c*) HAZ, and (*d*) BM.

Table I. Effect of Tool Rotational Rate and Welding Speed on the Grain Size (Mean Value ± SD) and Failure Load of FSLWed AZ31B-H24 Mg Alloy

Tool Rotational Rate (rpm)	Welding Speed (mm/s)	Weld Pitch (mm/rev)	Grain Size (*d*), μm				Failure Load (kN)
			BM	HAZ	TMAZ	SZ	
1000	20	1.2	4.25 ± 0.10*	4.63 ± 0.25	6.16 ± 0.14	7.46 ± 0.24	6.52
1500	20	0.8	—	5.31 ± 0.23	6.48 ± 0.19	8.59 ± 0.16	2.16
1500	10	0.4	—	6.15 ± 0.22	8.20 ± 0.06	9.57 ± 0.06	2.22

*The mean value and standard deviation (SD) for the BM were taken from all the values measured for the BM in different welding conditions.

the likelihood of crack formation in the SZ of the friction stir lap welds may remain similar. Similar intermetallic phases have been identified by Xiao *et al.*[39] in a resistance spot-welded AZ31-H24 Mg alloy.

B. Crystallographic Texture

The (0001), ($10\bar{1}0$), and ($10\bar{1}1$) pole figures determined from the FSLW joints at tool rotational rates of 1000 and 1500 rpm, and at welding speeds of 10 and 20 mm/s are shown in Figure 7 for the different locations. The BM shows a strong basal texture, where the basal plane (0001) normal was largely parallel to the normal direction (ND) with some grains tilted slightly toward the RD and the ($10\bar{1}0$) and ($10\bar{1}1$) directions were aligned or tilted in the TD (Figures 7(a) through (c)). It suggests that the (0001)$\langle 11\bar{2}0 \rangle$ texture component was mainly present in the current AZ31B-H24 BM. It has been reported that two major types of basal texture components, (0001)$\langle 11\bar{2}0 \rangle$ and (0001)$\langle 10\bar{1}0 \rangle$, are available, depending on the activation of the slip systems in the basal plane (either $\langle 11\bar{2}0 \rangle$ single slip or $\langle 10\bar{1}0 \rangle$ double slip oriented in the RD) in the Mg alloys.[40–42] Similarly, the (0001)$\langle 11\bar{2}0 \rangle$ texture component in the AZ31 Mg alloy has also been reported in References 43 through 48.

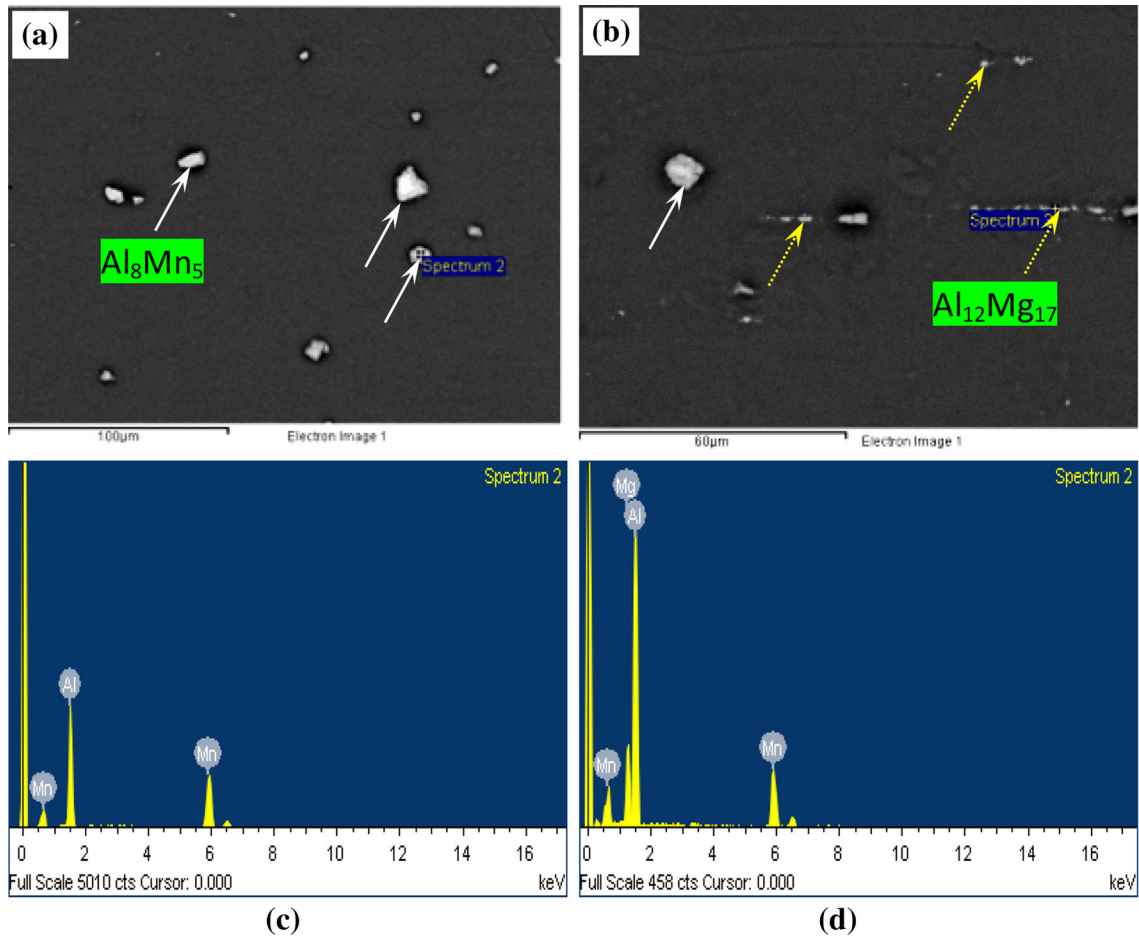After FSLW, the basal plane (0001) normal in the SZ became tilted slightly toward the TD, which was in

Fig. 5—Secondary electron imaging and EDS point analysis of the Al-Mn and Al-Mg particles: (a) coarse Al_8Mn_5 particles as indicated by arrows in the BM; (b) coarse Al_8Mn_5 and fine $Al_{12}Mg_{17}$ particles as indicated by arrows in the SZ; (c) EDS analysis of Al_8Mn_5 particles in the BM; and (d) EDS analysis of $Al_{12}Mg_{17}$ particles in the SZ.

Table II. EDS Analysis Results on the Particles Observed in the BM and SZ of FSLWed AZ31B-H24 Mg Alloy

Element	BM Particles	SZ	
		Large Particles	Small Particles
Al, K_α (at. pct)	61.4	34.4	63.5
Mn, K_α (at. pct)	38.6	9.6	36.5
Mg, K_α (at. pct)	—	56.0	—

direct contrast to the basal plane (0001) normal in the BM that was tilted slightly toward the RD (Figures 7(a) through (c)). This means that the relatively strong basal texture in the SZ resulted from the basal plane (0001) normal being largely parallel to the ND with only some grains slightly tilted in the TD. The occurrence of such a texture change in the SZ was attributed to the intense localized shear plastic flow near the top sheet surface that is a result of the material flow generated by the rotating tool on the AS of the weld during FSW. Since the preferential slip plane of the AZ31-H24 Mg alloy with an hcp structure is known to be the basal plane (0001) for plastic deformation at room temperature,[49] the change in the texture may affect the tensile

properties of the FSWed AZ31B-H24 Mg alloy as discussed later.

In the BM, the prismatic planes (10$\bar{1}$0) were oriented toward the TD in a concentric circular pattern at 90 deg from the center of the pole figure, indicating the formation of a partially basal fiber texture (c-axis in the ND), which is also known as crystallographic fibering produced by crystallographic reorientation of the grains during deformation.[50–52] The partially crystallographic fibering in the BM could also be seen from the pyramidal planes (10$\bar{1}$1) that formed an incomplete ring at approximately 45 deg from the center of the pole figure toward the TD, as shown in Figures 7(a) through (c). On the other hand, in the SZ most of the prismatic planes (10$\bar{1}$0) and pyramidal planes (10$\bar{1}$1) were oriented toward the RD, irrespective of the welding conditions (Figures 7(a) through (c)). These changes reflect a 30 deg rotation of the hcp unit cell with respect to the rolled sheet normal (or ND). It indeed suggests a texture transformation from the (0001)⟨11$\bar{2}$0⟩ texture component existing in the BM into the (0001)⟨10$\bar{1}$0⟩ texture component newly formed in the SZ after FSLW. Similar phenomena of texture change during compressive deformation of an extruded AM30 magnesium alloy were reported by Sarker and Chen,[42] where the two initial
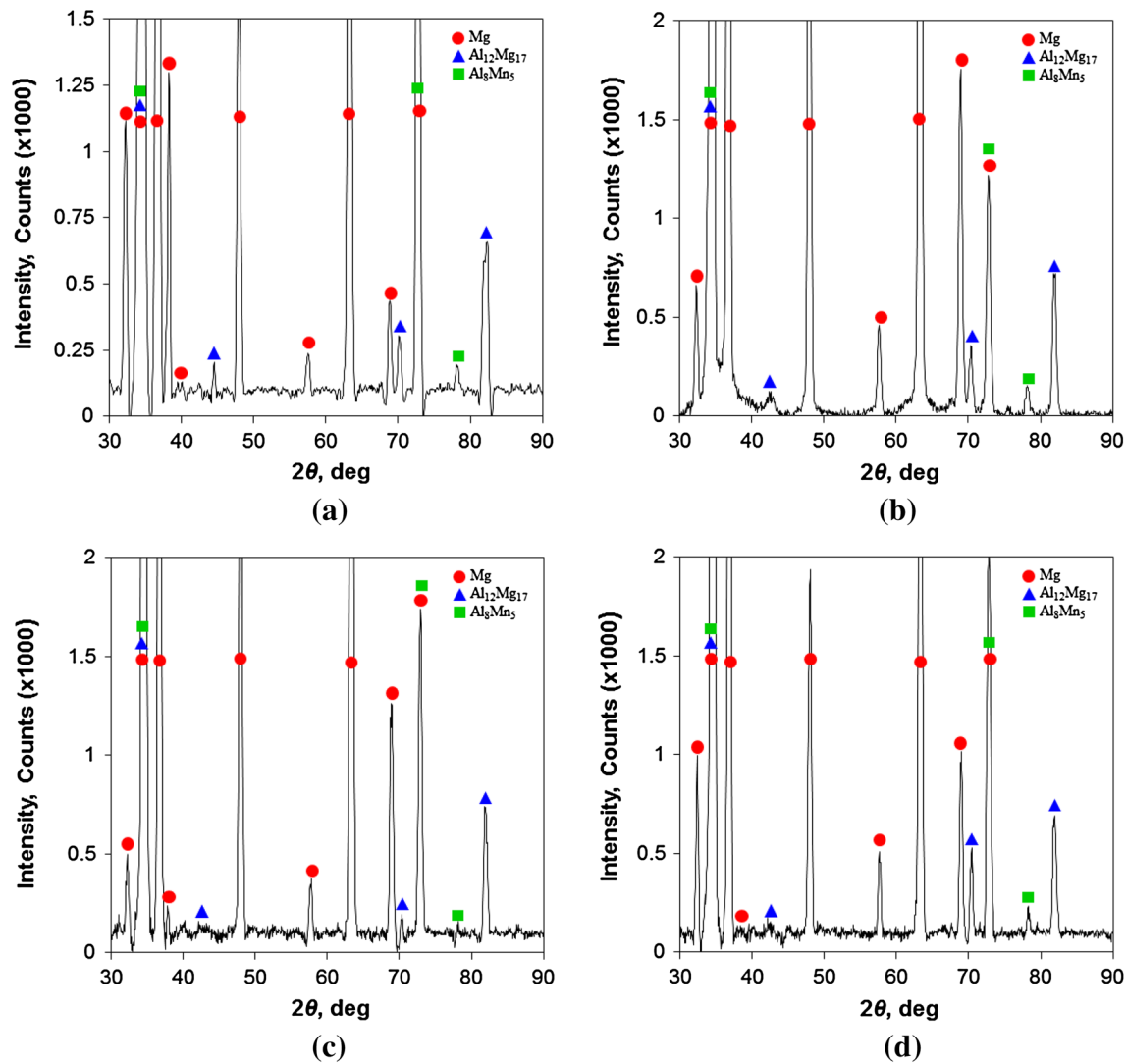
Fig. 6—X-ray diffraction patterns obtained from the top surface of (*a*) BM; (*b*) SZ of the FSLWed AZ31B-H24 Mg alloy at 1000 rpm and 20 mm/s; (*c*) SZ of the FSLWed AZ31B-H24 Mg alloy at 1500 rpm and 20 mm/s; and (*d*) SZ of the FSLWed AZ31B-H24 Mg alloy at 1500 rpm and 10 mm/s.

types of basal textures $\{0001\}\langle 2\bar{1}\bar{1}0\rangle$ and $\{0001\}\langle 10\bar{1}0\rangle$ were transformed into two new types of textures $\{\bar{1}2\bar{1}0\}\langle 0001\rangle$ and $\{01\bar{1}0\}\langle 0001\rangle$ during the compression, indicating that the *c*-axes of the hcp unit cells were always rotated toward the anti-compression direction due to the occurrence of extension twinning at room temperature. The texture change in the present FSLWed AZ31B-H24 Mg alloy, as shown in Figure 8, may be related to the localized shear plastic deformation *via* an intense circumferential stirring in the SZ likely through both twinning and dislocation slip due to the occurrence of elevated temperatures in the process. To better understand the texture change in the SZ after FSLW, a schematic illustration of an hcp unit cell showing the transformation of texture from $(0001)\langle 11\bar{2}0\rangle$ component (BM) into the $(0001)\langle 10\bar{1}0\rangle$ component (SZ) is shown in Figure 8. Let us start with the (0001) basal plane of an hcp unit cell in the BM where the six prismatic planes are perpendicular to the rolled sheet/paper plane and numbered from 1 to 6. Based on the pole figures of

BM shown in Figure 7, the initial unit cell in the BM should be positioned in such a way that the prismatic planes (3 and 6) are parallel to the RD direction and perpendicular to the TD (Figure 8(a)). As mentioned above, due to the intense circumferential stirring action occurring during FSLW, the $(0001)\langle 10\bar{1}0\rangle$ type of basal texture was formed in the SZ (Figure 7), where both the prismatic planes $(10\bar{1}0)$ and pyramidal planes $(10\bar{1}1)$ exhibited a 30 deg clockwise rotation with respect to the paper plane normal (Figure 8(b)). However, due to the sixfold symmetry of the hcp unit cell, this particular type of texture can be repeated in a certain rotation of the unit cell (Figures 8(c), (d)). The possible angles of rotation of a unit cell during FSLW can be expressed as follows:

$$\theta = \theta_i + (n-1) \times 60 \text{ deg}, \qquad [1]$$

where θ is the angle of rotation, θ_i is the initial angle of rotation (*i.e.*, 30 deg), and *n* is an integer ($n = 1, 2, 3,$
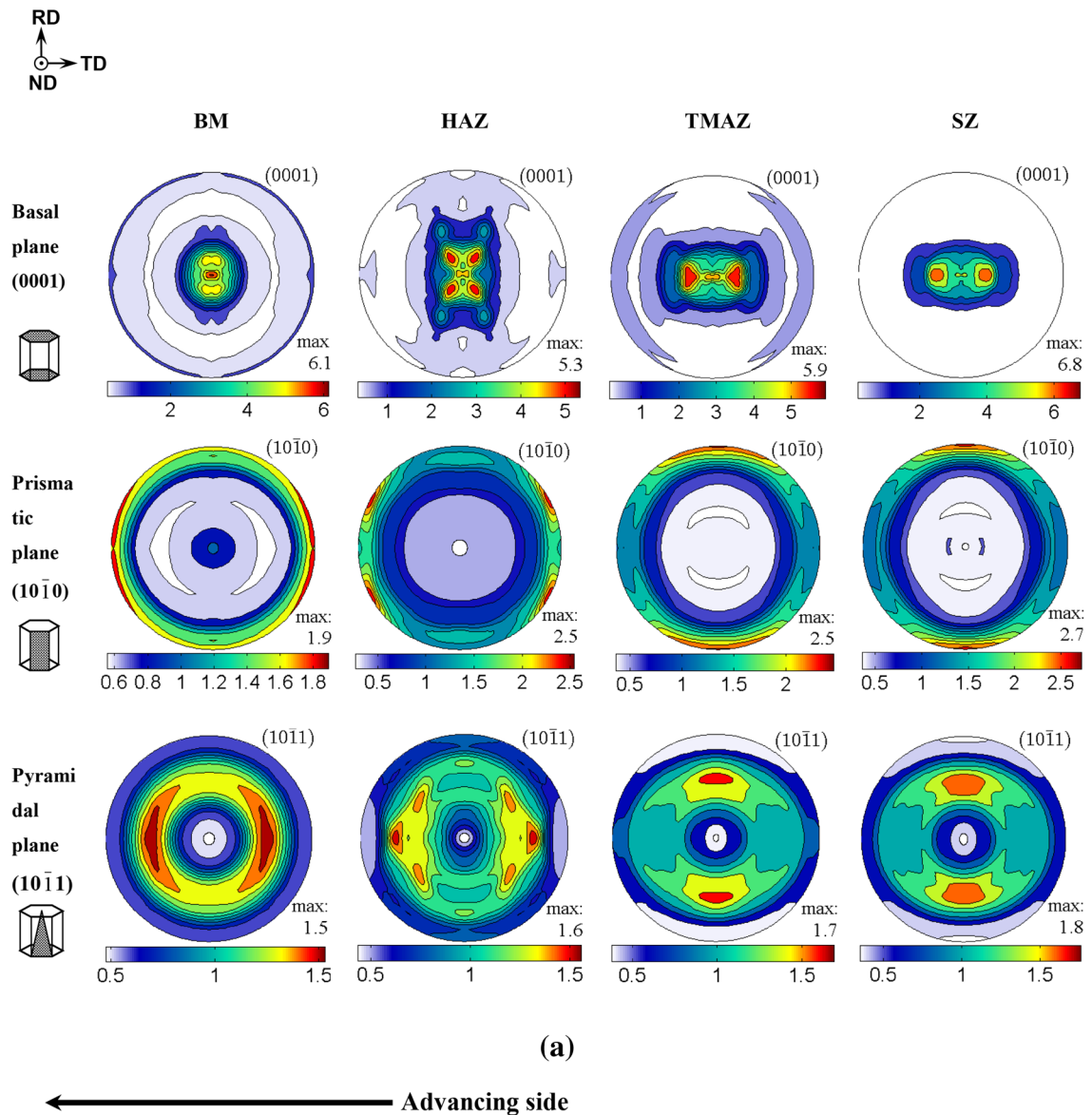
Fig. 7—(0001) basal, (10$\bar{1}$0) prismatic, and (10$\bar{1}$1) pyramidal plane pole figures of the FSLWed AZ31B-H24 Mg alloy obtained from the SZ, TMAZ, HAZ, and BM at (*a*) 1000 rpm and 20 mm/s, (*b*) 1500 rpm and 20 mm/s, and (*c*) 1500 rpm and 10 mm/s (Color figure online).

…). The present finding is also supported by the work of Park *et al.*[27] on the FSW of 6.3-mm thick wrought AZ61 Mg alloy that revealed that both the prismatic and pyramidal planes were oriented in the RD, which was attributed to the intense stirring/plastic flow in the stirred region. In Mg alloys, the critical resolved shear stress (CRSS) for the basal slip system is much lower than that for the prismatic and pyramidal slip systems at room temperature.[53] Therefore, the basal slip may dominate the plastic deformation of the FSWed Mg alloy at room temperature, while both the basal and non-basal slip systems may be operational during hot deformation at temperatures higher than about 600 K (327 °C).[54] Noticeably, the crystallographic orientation changes in the HAZ were smaller; the HAZ had a texture more similar to the BM in the basal plane (0001),

and the prismatic (10$\bar{1}$0) and pyramidal planes (10$\bar{1}$1) were mainly oriented toward the TD also, as shown in Figures 7(a) through (c). Meanwhile, the TMAZ texture basically lay in-between those of the HAZ (or BM) and SZ, it was nonetheless more similar to the SZ texture, *i.e.*, the (0001)⟨10$\bar{1}$0⟩ texture (Figures 7(a) through (c)).

The effect of the tool rotational rate and welding speed on the texture is also shown in Figures 7(a) through (c), where the (0001), (10$\bar{1}$0), and (10$\bar{1}$1) pole figures were obtained from the center of the SZ in the friction stir lap welds joined at 1000 rpm and 20 mm/s (Figure 7(a)), 1500 rpm and 20 mm/s (Figure 7(b)), and 1500 rpm and 10 mm/s (Figure 7(c)). As mentioned above, these pole figures indicate that similar texture changes occurred in the AZ31B-H24 Mg alloy after FSLW. However, the relative texture intensity in the
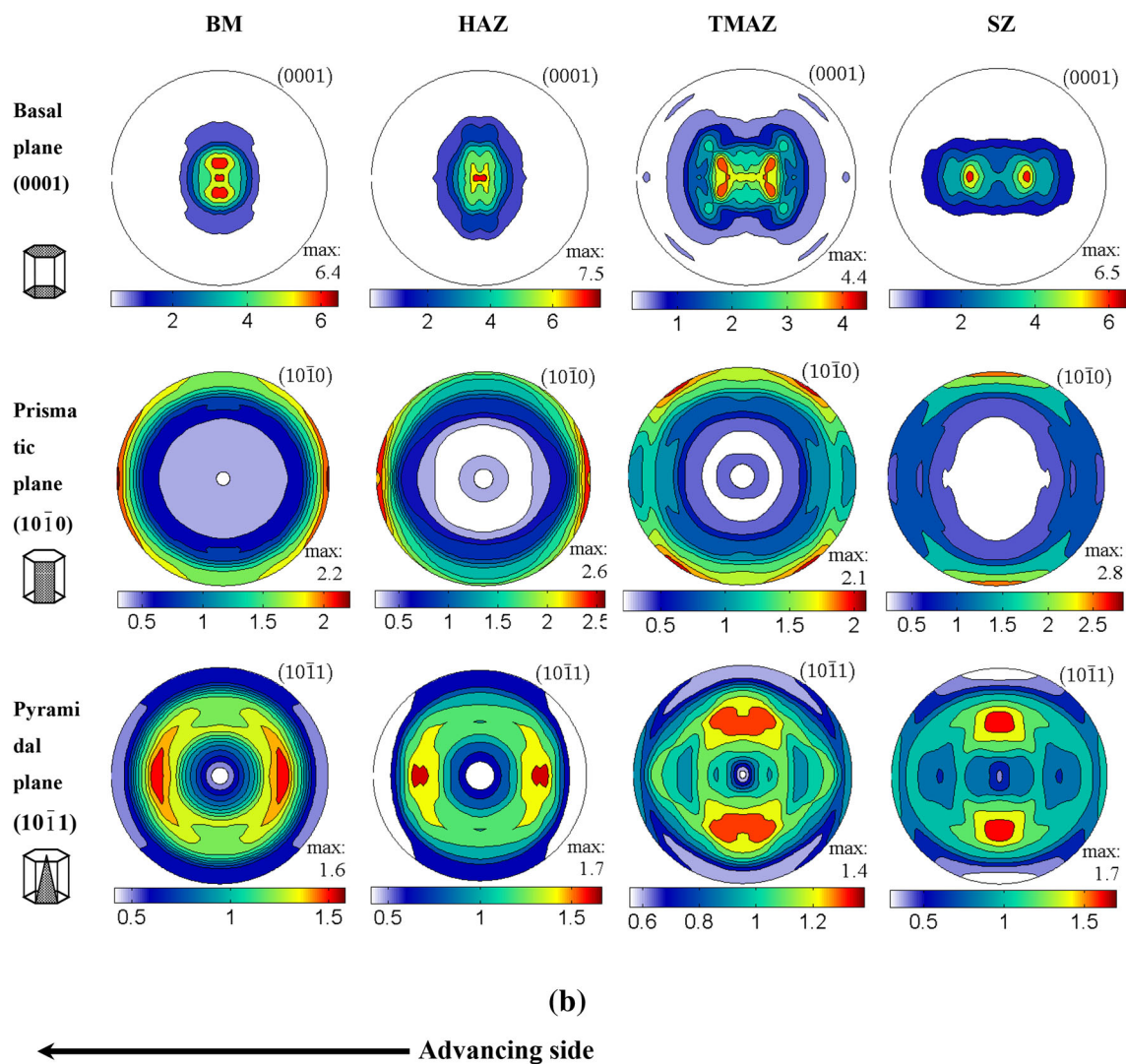
(b)

← Advancing side

Fig. 7—continued.

SZ was different, which is summarized in Table III with the values given in multiples of random distribution (MRD). It is clear that after FSLW the intensity of the basal plane (0001), prismatic plane (10$\bar{1}$0), and pyramidal plane (10$\bar{1}$1) in the SZ all increased at a welding speed of 20 mm/s and a rotational rate of 1000 or 1500 rpm, in comparison with the BM. Specifically, the maximum intensity of (0001) poles in the SZ was observed to decrease with increasing rotational rate or decreasing welding speed. This was due to the fact that the higher tool rotational rate (*i.e.*, 1500 rpm) or lower welding speed (*i.e.*, 10 mm/s) generated a higher temperature in the SZ, which then resulted in more complete dynamic recrystallization. This would in turn lead to a progressively weaker texture or more random orientation when the tool rotation rate increases from 1000 to 1500 rpm and the welding speed decreases from 20 to 10 mm/s. Overall, these findings are supported by Patel et al.[55] who used an ultrasonic spot welding technique to lap weld AZ31B-H24 Mg alloy and reported that the crystallographic texture corresponded to the change in

the deformation and recrystallization mechanisms. Similar observations were also reported for FSWed AZ31B billets and extruded plates,[28] where a more random orientation at higher rotational rates was observed.

C. Microhardness

Figure 9 shows the Vickers microhardness profiles across the SZ of the FSLWed AZ31B-H24 Mg alloy. For all the welds joined at different tool rotational rates and welding speeds, the hardness profiles were measured along the weld cross-section at the mid-thickness of the top sheet. In each welding condition, a hardness trough was observed with higher values in the BM relative to those in the HAZ, TMAZ, and SZ. Specifically, the hardness decreased gradually from about 70 to 75 HV in the BM to approximately 55 to 60 HV at the center of the SZ of the welds, representing a decrease of up to ~25 pct. This hardness change can be attributed to the effect of the welding parameters on the
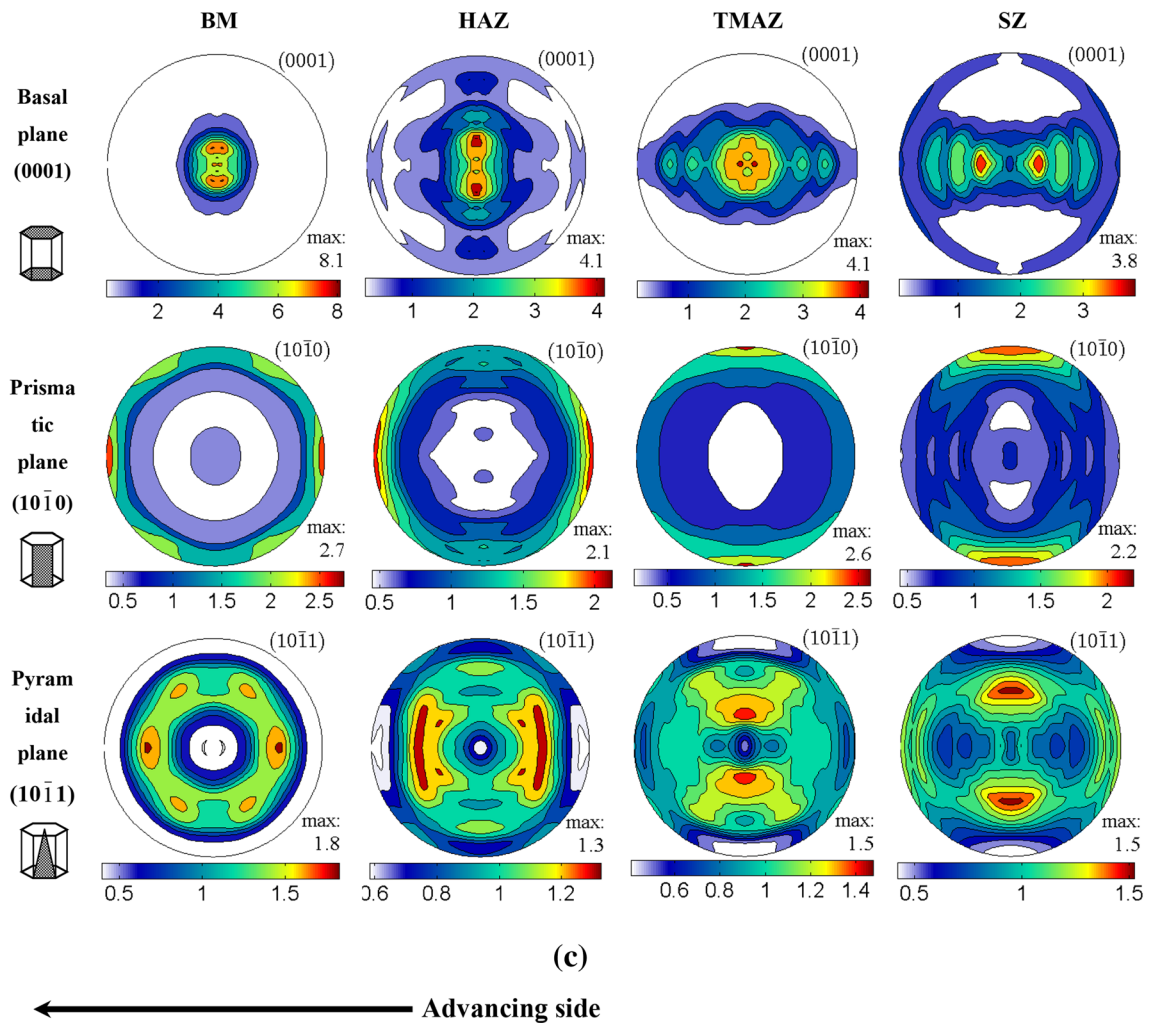
(c)

← **Advancing side**

Fig. 7—continued.

heat input during FSW and the resulting microstructural evolution (*i.e.*, grain shape, size, and texture) in the SZ, as depicted previously in Figures 2, 3, and 4 and tabulated in Table I. Specifically, at a constant welding speed of 20 mm/s, an increase in the rotational rate from 1000 to 1500 rpm was observed to decrease the average value of the hardness in the SZ from 60 HV to about 55 HV, inevitably due to the greater heat input and coarser SZ grain size in the latter welding condition. At 1500 rpm, a decrease in the welding speed from 20 to 10 mm/s was observed to reduce the average hardness in the SZ slightly further to roughly 52 HV. Moreover, within different regions of the lap weld, there was a progressive increase in the grain size from the BM to the SZ as tabulated in Table I, which corresponded well to the observed evolution in the microhardness, as shown in Figure 9.

Another reason for the lower hardness in the SZ may be related to the texture variation. During FSW, plastic material flow occurred in the SZ and resulted in a more random orientation (Figures 7(a) through (c)) relative to that in the BM, *i.e.*, the basal plane (0001) rotated

around the periphery of the stirring pin, thereby producing a soft region around the SZ.[27] As a result, the low hardness value observed in the SZ of the FSLWed joints in the present study may also be associated with the local texture variation.

D. *Tensile Shear Properties*

Figure 10 shows typical load-displacement curves of the FSLWed AZ31B-H24 Mg alloy joined at different tool rotational rates and welding speeds and then tensile shear tested at a crosshead speed of 1 mm/min. Significant changes in the failure load for the friction stir lap welds joined in the different conditions (Table I) were observed. Specifically, the friction stir lap weld joined at a rotational rate of 1000 rpm and welding speed of 20 mm/s was noted to have the highest failure load of 6.52 kN. At a constant welding speed of 20 mm/s, an increase in the tool rotation rate to 1500 rpm resulted in a significant decrease (58 pct) in the failure load to 2.16 kN (Figure 10; Table I). In contrast, a decrease in the welding speed from 20 to 10 mm/s at a constant tool

rotational rate of 1500 rpm gave almost the same failure load (*i.e.*, 2.16 and 2.22 kN).

A decrease in the failure load with increasing tool rotational rate (1000 to 1500 rpm) at a constant welding speed of 20 mm/s can be reasoned on the basis of the heat input during FSLW and the resulting increase in grain size in the weldment. As grain boundaries are major obstacles to dislocation slip in the material, a smaller grain size would more effectively hinder dislocation motion and render a higher resistance to localized plastic deformation that then culminates to a higher failure load. However, the heat input and grain size are evidently not the only factors influencing the

failure load as evidenced from the 1500 rpm and 10 mm/s FSLW condition. That is, both the heat input and grain size are higher in the 1500 rpm and 10 mm/s FSLW condition relative to the 1500 rpm and 20 mm/s condition, but their failure loads are similar. One explanation for this occurrence may be related to the nature of hooking defects in the friction stir lap welds as reported in Reference 26. In particular at 1000 rpm and 10 mm/s, the relatively "cold" weld conditions led to almost complete elimination of the hooking defect, which was quite prominent in the AZ31B-H24 Mg alloy friction stir lap welds assembled at 1500 rpm with an advancing speed of 10 or 20 mm/s.

Besides the influence of these microstructural changes on the properties, crystallographic texture/orientation distribution can also strongly influence the flow stress behavior during tensile loading, since the plastic deformation arises mainly from the dislocation slip on the closed-packed basal planes with the minimum CRSS.[1] When the FSLWed joints were deformed at room temperature along the RD (loading direction), the basal planes had a tendency to rotate and lie parallel to the rolled sheet surface and the tensile axis. This may be a result of the twinning and dislocation activity in
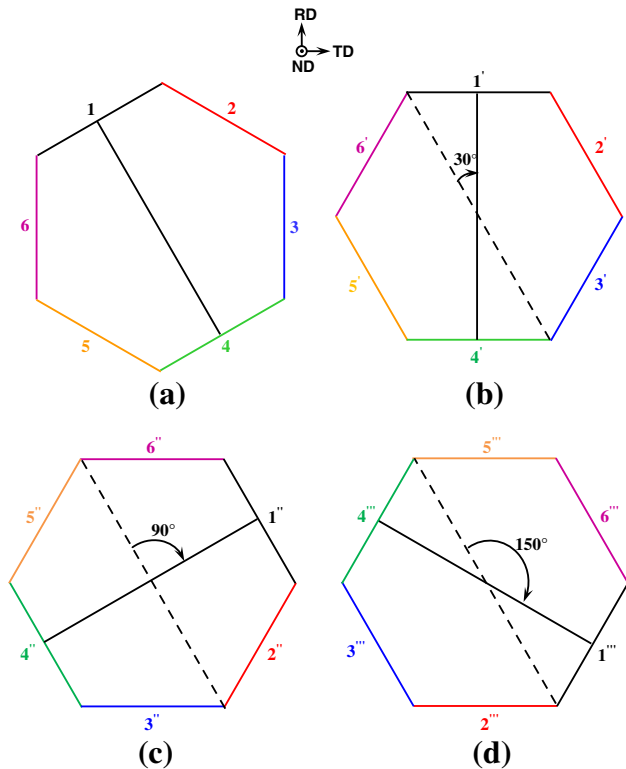

Fig. 8—Schematic illustration of the basal plane (0001) in an hcp unit cell, where the six prismatic planes {$10\bar{1}0$} are perpendicular to the paper plane and indicated by 1, 2,…, 6, showing the change of texture from $(0001)\langle11\bar{2}0\rangle$ component (BM) into the $(0001)\langle10\bar{1}0\rangle$ component (SZ), (*a*) BM, and (*b* through *d*) SZ with different angles of rotation after FSLW.
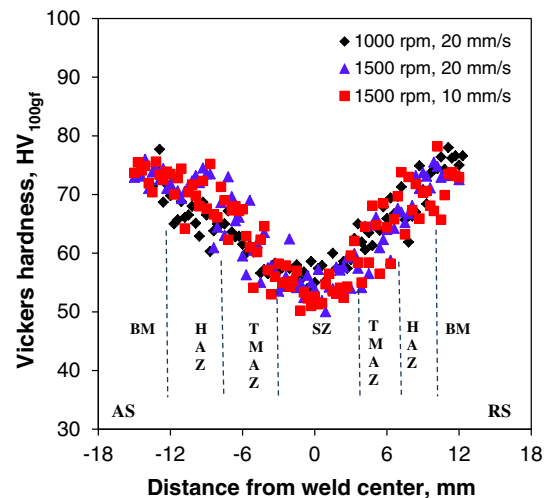

Fig. 9—Typical microhardness profiles at the mid-thickness of the top sheet in the FSLWed AZ31B-H24 Mg alloy assembled at different tool rotational rates and welding speeds (where AS is the advancing side and RS is the retreating side).

Table III. Effect of Tool Rotational Rate and Welding Speed on the Maximum Pole Intensities (in MRD) in FSLWed AZ31B-H24 Mg Alloy

	Rotational Rate: 1000 rpm Welding Speed: 20 mm/s			Rotational Rate: 1500 rpm Welding Speed: 20 mm/s			Rotational Rate: 1500 rpm Welding Speed: 10 mm/s		
	(0001) Basal Plane	($10\bar{1}0$) Prismatic Plane	($10\bar{1}1$) Pyramidal Plane	(0001) Basal Plane	($10\bar{1}0$) Prismatic Plane	($10\bar{1}1$) Pyramidal Plane	(0001) Basal Plane	($10\bar{1}0$) Prismatic Plane	($10\bar{1}1$) Pyramidal Plane
BM	6.1	1.9	1.5	6.4	2.2	1.6	8.1	2.7	1.8
HAZ	5.3	2.5	1.6	7.5	2.6	1.7	4.1	2.1	1.3
TMAZ	5.9	2.5	1.7	4.4	2.1	1.4	4.1	2.6	1.5
SZ	6.8	2.7	1.8	6.5	2.8	1.7	3.8	2.2	1.5

favorably oriented grains as well as twin-dislocation interactions during deformation.[42,56–59] For instance, in comparison to the welding conditions at a tool rotation rate of 1500 rpm, the stronger intensity of the basal plane (0001) present in the higher hardness SZ of the 1000 rpm and 20 mm/s condition (*i.e.*, 6.8 *vs* 6.5 MRD and 3.8 MRD in Table III or Figure 7) suggests that the basal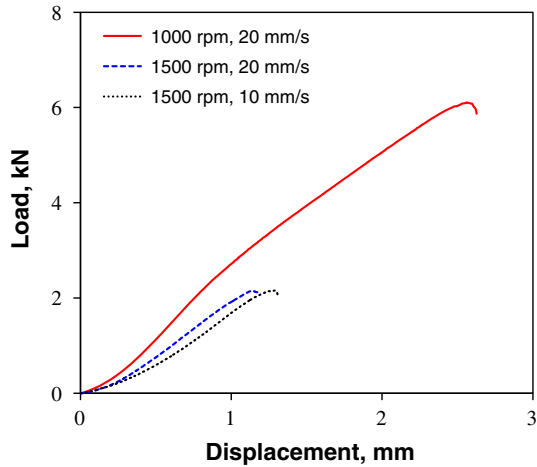 planes of more grains were oriented parallel to the rolled sheet surface, *i.e.*, the basal plane normal of more grains was perpendicular to the sheet surface. While performing the tensile test in such a case, plastic deformation becomes more difficult in the SZ, which has the lowest hardness in all the FSLWed joints
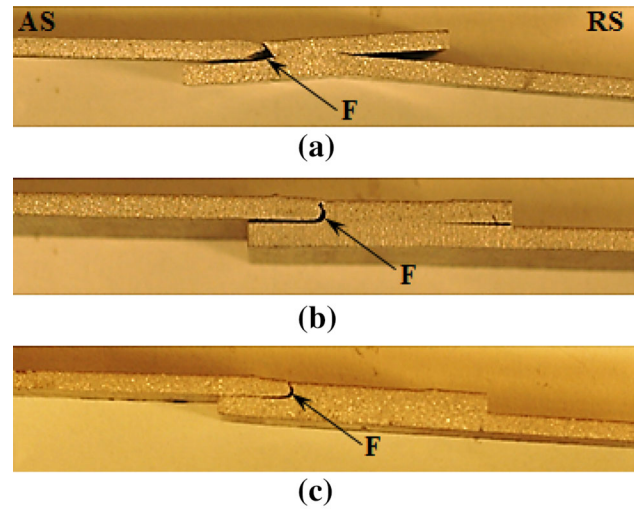

Fig. 10—Typical load *vs* displacement curves of the FSLWed AZ31B-H24 Mg alloy assembled at different tool rotational rates and welding speeds.

Fig. 11—The fracture location, demarcated by the symbol "**F**", in the fractured tensile samples of FSLWed AZ31B-H24 Mg alloy obtained at various combinations of tool rotational rates and welding speeds: (*a*) 1000 rpm-20 mm/s, (*b*) 1500 rpm-20 mm/s, and (*c*) 1500 rpm-10 mm/s.
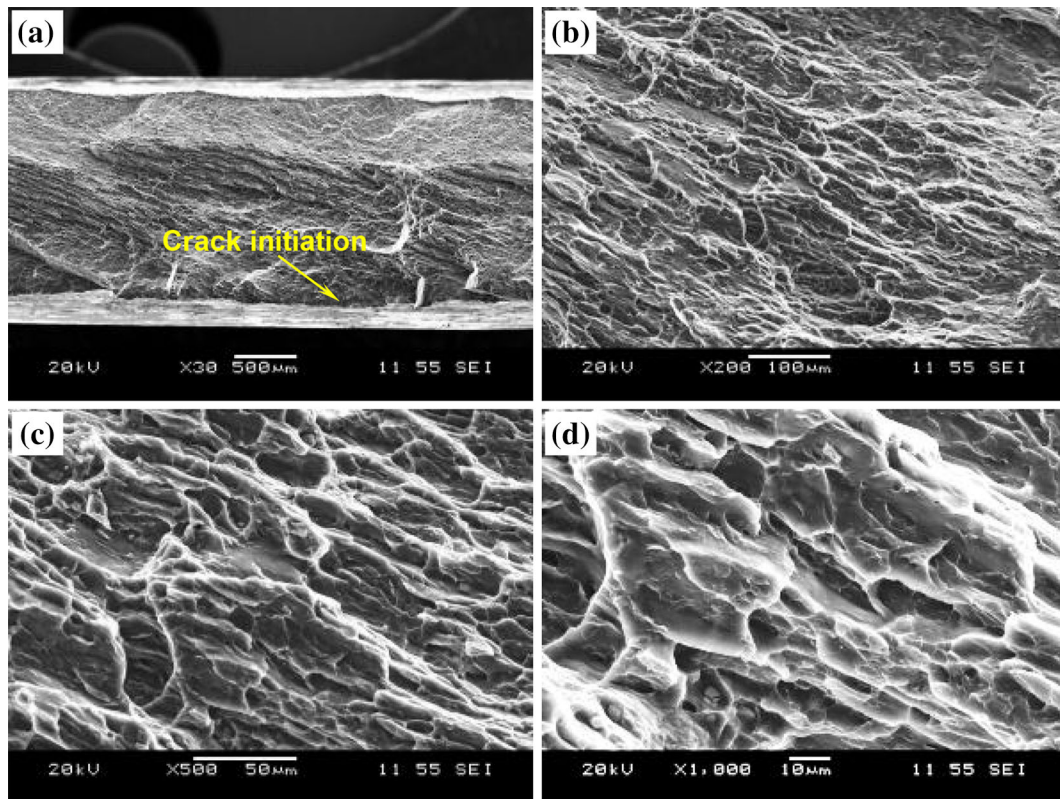

Fig. 12—Typical SEM images of the tensile shear fracture surface of a FSLWed AZ31B-H24 Mg alloy assembled at a rotational rate of 1000 rpm and a welding speed of 20 mm/s: (*a*) overall view of a fracture surface and crack initiation site, (*b*) crack initiation site at a higher magnification, (*c*) crack propagation region at a lower magnification, and (*d*) crack propagation region at a higher magnification.

(Figure 9), since the Schmid factor $m = \cos\phi \cos\lambda$[60] is nearly zero due to the basal (0001) slip plane of most grains being parallel to the rolled sheet surface; ϕ is the angle between the normal to the slip plane and the tensile axis, and λ is the angle between the slip direction and the tensile axis. As a result, an increasingly higher load is needed to continue the tensile deformation until failure occurs, leading to a higher failure load in the case of 1000 rpm and 20 mm/s welding condition (Table I).

Figure 11 shows the fractured tensile samples of the FSLWed AZ31B-H24 Mg alloy, which were joined at different tool rotational rates and welding speeds. It is clear that the tensile failure of the lap welds occurred basically in the vicinity of the SZ/TMAZ on the AS. This region experienced the maximum tensile stresses during tensile shear testing and had severe hooking defects, which can not only reduce the effective sheet thickness but also cause stress/strain concentration.[26] In addition, it was reported that the texture distribution of the basal plane (0001) can influence the tensile failure of a FSWed AZ61 Mg alloy.[54] As seen in Figures 7(a) through (c), the texture distribution of the basal plane (0001) from the BM to the TMAZ and SZ of the FSLWed AZ31B-H24 Mg alloy has changed, i.e., the c-axes of the hcp unit cells in most grains were rotated from the orientation distributed slightly in the RD in the BM to that distributed in the TD in the TMAZ and SZ. In the deformation of Mg alloys at room temperature, both extension twinning and basal slip may normally occur, since both deformation modes have a relatively lower CRSS at room temperature.[61] However, which mode may be activated is dependent on the direction of the applied load during tension. In general, the extension twinning occurs when a tensile load is applied along the c-axes of an hcp unit cell, or when a compressive load is applied perpendicularly to the c-axes.[62–65] As mentioned above, the c-axes of the hcp unit cells in the TMAZ and SZ are mainly distributed in the TD direction, i.e., being always perpendicular to the tensile loading direction (or RD). In this case only basal slip, rather than extension twinning, would be activated along the RD in the TMAZ/SZ during the tensile tests. Magnesium alloys deformed in the mode of basal slip exhibited a higher yield strength than those deformed in the mode of extension twinning.[66,67] For instance, the yield strength was observed to be considerably (over 2 times) higher than that obtained in the deformation mode of extension twinning, as reported recently by Sarker and Chen[68] in an extruded AM30 Mg alloy. Therefore, the TMAZ and SZ would be expected to be strengthened locally by the texture distribution after FSW. As such, the texture distribution has little influence on the tensile failure location of the FSLWed AZ31B-H24 Mg alloy joints. Therefore, the fracture around the TMAZ and SZ on the AS (Figure 11) was mainly attributed to the two major dominant factors: (i) maximum tensile stress experienced and (ii) the presence of the severe hooking defects.
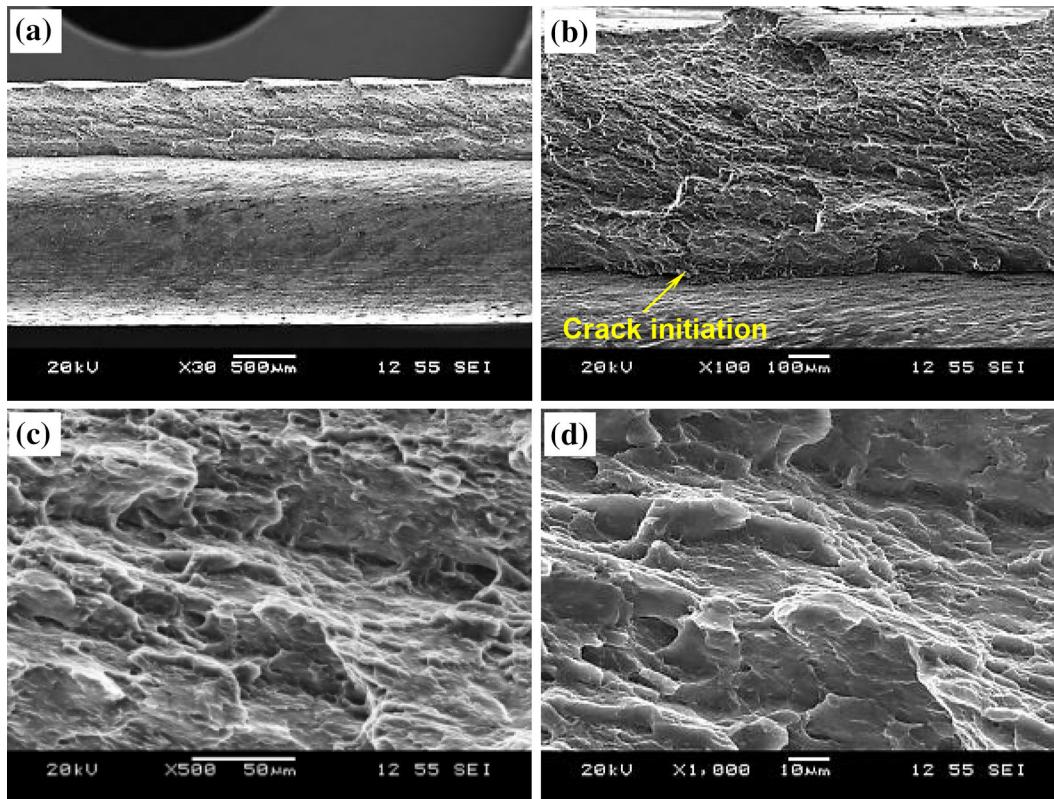

Fig. 13—Typical SEM images of the tensile fracture surface of a FSLWed AZ31B-H24 Mg alloy assembled at a rotational rate of 1500 rpm and a welding speed of 20 mm/s: (a) overall view of a fracture surface, (b) crack initiation site, (c) crack propagation region at a lower magnification, and (d) crack propagation region at a higher magnification.
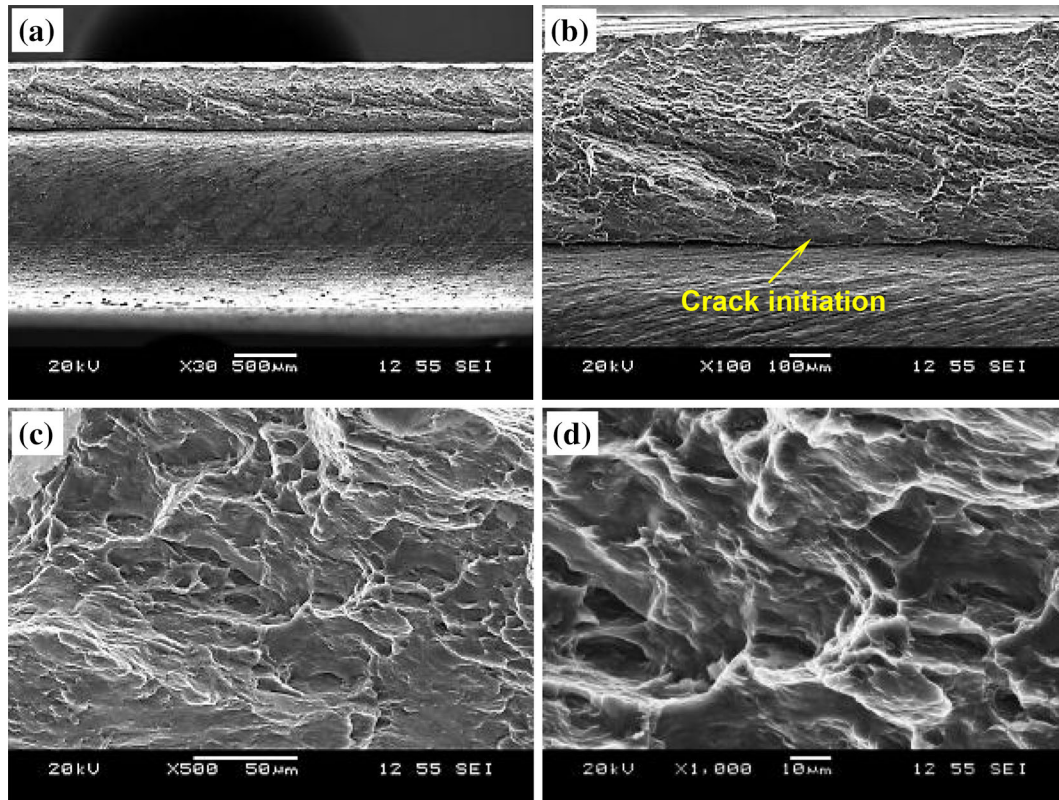
Fig. 14—Typical SEM images of the tensile fracture surface of a FSLWed AZ31B-H24 Mg alloy assembled at a rotational rate of 1500 rpm and a welding speed of 10 mm/s: (*a*) overall view of a fracture surface, (*b*) crack initiation site, (*c*) crack propagation region at a lower magnification, and (*d*) crack propagation region at a higher magnification.

E. *Fractography*

After tensile testing, the fractured surfaces of the samples were examined using SEM. Figures 12, 13, and 14 show the secondary electron images of the tensile fracture surfaces of the FSLWed joints assembled at the different tool rotational rates and welding speeds. The tensile fracture surface characteristics appeared to be relatively similar in all the welding conditions. Figures 12(a), 13(b), and 14(b) show that crack initiation occurred essentially from the local stress concentration due to the welding defects, such as the hooking defect in the SZ/TMAZ region in the AS or near the surface,[23] as indicated by the arrows. Such welding defects were considered to form due to excessive heat input during FSLW.[22] Figures 12(c) and (d) show the crack propagation regions in the 1000 rpm and 20 mm/s condition, which exhibited some characteristics of ductile fracture (*e.g.*, parabolic dimples from the shear loading). In contrast, Figures 13(c) and (d) and 14(c) and (d) show the crack propagation regions in the 1500 rpm at 10 and 20 mm/s conditions, respectively, where the fracture characteristics contained both facets and dimples. The inherently greater ductility and load-bearing capacity of the welds manufactured at 1000 rpm and 20 mm/s as reflected in the tensile shear properties and fracture behavior was linked to the microstructural evolutions during FSLW, including the defects, grain size, phase constituents and texture, as described previously.

IV. CONCLUSIONS

1. Under the welding conditions examined in this work, the SZ, thermomechanically affected zone, and heat-affected zone exhibited grain coarsening relative to the base material microstructure. In addition, the grain size in each region of the weldment increased with increasing heat input (*i.e.*, increasing tool rotational rate and decreasing welding speed).

2. Microstructural characterization showed that the stir zone of the friction stir lap welds contained Al_8Mn_5 and β-$Mg_{17}Al_{12}$ particles, similar to that in AZ31B-H24 Mg alloy BM.

3. The base metal contained a strong crystallographic texture of type $(0001)\langle11\bar{2}0\rangle$, with the basal planes (0001) largely parallel to the rolled sheet surface (or slightly tilted toward the RD) and the $\langle11\bar{2}0\rangle$ directions aligned in the RD of the sheet. After FSLW, the texture in the stir zone (and thermomechanically affected zone) became another type of texture $(0001)\langle10\bar{1}0\rangle$, where the basal planes (0001) were slightly tilted toward the transverse direction (TD), and the prismatic planes $(10\bar{1}0)$ and pyramidal planes $(10\bar{1}1)$, exhibiting a certain degree of fiber-like textures, had a 30 deg $+ (n - 1) \times$ 60 deg rotation ($n = 1, 2, 3, \ldots$) with respect to the rolled sheet normal, with the situation of HAZ texture laying in-between those of base metal and thermomechanically affected zone or stir zone. This was attributed to the intense circumferential stirring/shear plastic flow in the vicinity of the pin surface.

4. With increasing tool rotational rate and decreasing welding speed, the maximum intensity of basal poles (0001) in the stir zone decreased due to the higher heat input during friction stir lap welding, which would allow a higher degree of dynamic recrystallization to completion and thereby render a weaker or more random texture.

5. A hardness trough was observed in the friction stir lap welds of AZ31B-H24 Mg alloy; the lowest hardness values, approximately 72 to 82 pct of the base metal hardness depending on the welding conditions, occurred in the stir zone and were related to the microstructural features, including grain size and texture.

6. In comparison to the texture distribution, the tool rotational rate and welding speed had a strong effect on the failure load of the friction stir lap welds. Based on the conditions applied in the present work, a combination of relatively high welding speed (20 mm/s) and low tool rotational rate (1000 rpm) led to a high failure load. This was attributed to the (i) low heat input that limited the grain coarsening, (ii) high intensity of the basal poles in the stir zone, and (iii) small hooking defect.

7. The texture distribution was reasoned to locally strengthen the thermomechanically affected zone and stir zone and thus the tensile failure, which occurred at the interface of the thermomechanically affected zone and stir zone on the AS, was mainly attributed to the maximum tensile stress experienced during the tensile testing and the presence of the severe hooking defects.

REFERENCES

1. T.M. Pollock: *Science*, 2010, vol. 328, pp. 986–87.
2. S.J. Davis, K. Caldeira, and H.D. Matthews: *Science*, 2010, vol. 329, pp. 1330–33.
3. M. Wise, K. Calvin, A. Thomson, L. Clarke, B. Bond-Lamberty, R. Sands, S.J. Smith, A. Janetos, and J. Edmonds: *Science*, 2009, vol. 324, pp. 1183–86.
4. W.G. Agnew: *Science*, 1974, vol. 183, pp. 254–56.
5. L.R. Kump: *Nature*, 2002, vol. 419, pp. 188–90.
6. J. Murray and D. King: *Nature*, 2012, vol. 481, pp. 433–35.
7. D.A. Howey: *Nat. Clim. Change*, 2012, vol. 2, pp. 28–29.
8. D. Shindell, G. Faluvegi, M. Walsh, S.C. Anenberg, R.V. Dingenen, N.Z. Muller, J. Austin, D. Koch, and G. Milly: *Nat. Clim. Change*, 2011, vol. 1, pp. 59–66.
9. H.J. Kim, G.A. Keoleian, and S.J. Skerlos: *J. Ind. Ecol.*, 2011, vol. 15, pp. 64–80.
10. H.J. Kim, C. McMillan, G.A. Keoleian, and S.J. Skerlos: *J. Ind. Ecol.*, 2010, vol. 14, pp. 929–46.
11. S. Begum, D.L. Chen, S. Xu, and A.A. Luo: *Mater. Sci. Eng. A*, 2009, vol. A517, pp. 334–43.
12. J.F. Nie, Y.M. Zhu, J.Z. Liu, and X.Y. Fang: *Science*, 2013, vol. 340, pp. 957–60.
13. Q. Yu, J. Zhang, Y. Jiang, and Q. Li: *Int. J. Fatigue*, 2011, vol. 33, pp. 437–47.
14. Q. Yu, J. Zhang, Y. Jiang, and Q. Li: *Int. J. Fatigue*, 2012, vol. 36, pp. 47–58.
15. J.B. Jordon, J.B. Gibson, M.F. Horstemeyer, H.E. Kadiri, J.C. Baird, and A.A. Luo: *Mater. Sci. Eng. A*, 2011, vol. 528, pp. 6860–71.
16. X. Cao and M. Jahazi: *Mater. Des.*, 2009, vol. 30, pp. 2033–42.
17. N. Afrin, D.L. Chen, X. Cao, and M. Jahazi: *Mater. Sci. Eng. A*, 2008, vol. 472, pp. 179–86.
18. H.B. Chen, K. Yan, T. Lin, S.B. Chen, C.Y. Jiang, and Y. Zhao: *Mater. Sci. Eng. A*, 2006, vol. 433, pp. 64–69.
19. R.S. Mishra and Z.Y. Ma: *Mater. Sci. Eng. R*, 2005, vol. 50, pp. 1–78.
20. S.H. Chowdhury, D.L. Chen, S.D. Bhole, X. Cao, and P. Wanjara: *Metall. Mater. Trans. A*, 2013, vol. 44A, pp. 323–36.
21. S.H. Chowdhury, D.L. Chen, S.D. Bhole, X. Cao, and P. Wanjara: *Mater. Sci. Eng. A*, 2012, vol. 556, pp. 500–509.
22. C. Liu, D.L. Chen, S. Bhole, X. Cao, and M. Jahazi: *Mater. Charact.*, 2009, vol. 60, pp. 370–76.
23. S.M. Chowdhury, D.L. Chen, S.D. Bhole, X. Cao, E. Powidajko, D.C. Weckman, and Y. Zhou: *Mater. Sci. Eng. A*, 2010, vol. 527, pp. 2951–61.
24. A.W. Tayon, S.M. Domack, K.E. Hoffman, and S.J. Hales: *Metall. Mater. Trans. A*, 2013, vol. 44A, pp. 4906–913.
25. X. Cao and M. Jahazi: *Proceedings of the 8th International Conference on "Trends in Welding Research"*, S.A. David, T. DebRoy, J.N. DuPont, T. Koseki, and H.B. Smart, eds., ASM International, Materials Park, OH, 2009.
26. B.S. Naik, D.L. Chen, X. Cao, and P. Wanjara: *Metall. Mater. Trans. A*, 2013, vol. 44A, pp. 3732–46.
27. S.H.C. Park, Y.S. Sato, and H. Kokawa: *Metall. Mater. Trans. A*, 2003, vol. 34A, pp. 987–94.
28. C.I. Chang, C.J. Lee, and J.C. Huang: *Scripta Mater.*, 2004, vol. 51, pp. 509–14.
29. W. Woo, H. Choo, D.W. Brown, P.K. Liaw, Z. Feng, M.B. Prime, and Z. Feng: *Scripta Mater.*, 2006, vol. 54, pp. 1859–64.
30. R. Fonda and J. Bingert: *Metall. Mater. Trans. A*, 2004, vol. 35A, pp. 1487–99.
31. D. Field, T. Nelson, Y. Hovanski, and K. Jata: *Metall. Mater. Trans. A*, 2001, vol. 32A, pp. 2869–77.
32. F. Bachmann, R. Hielscher, and H. Schaeben: *Trans. Tech. Publ.*, 2010, vol. 160, pp. 63–8.
33. ASTM International Standard ASTM D3164-03: *Standard Test Method for Strength Properties of Adhesively Bonded Lap-Shear Sandwich Joints in Shear by Tensile Loading*, 2003.
34. N. Afrin, D.L. Chen, X. Cao, and M. Jahazi: *Scripta Mater.*, 2007, vol. 57, pp. 1004–07.
35. M. Fairman, N. Afrin, D.L. Chen, X.J. Cao, and M. Jahazi: *Can. Metall. Quart.*, 2007, vol. 46, pp. 425–32.
36. M. Ohno and R. Schmid-Fetzer: *Z. Metallkd.*, 2005, vol. 96, pp. 857–69.
37. C.Y. Liu, R. Jing, Q. Wang, B. Zhang, Y.Z. Jia, M.Z. Ma, and R.P. Liu: *Mater. Sci. Eng. A*, 2012, vol. 558, pp. 510–16.
38. J. Yan, Z. Xu, Z. Li, L. Li, and S. Yang: *Scripta Mater.*, 2005, vol. 53, pp. 585–89.
39. L. Xiao, L. Liu, Y. Zhou, and S. Esmaeili: *Metall. Mater. Trans. A*, 2010, vol. 41A, pp. 1511–22.

40. G. Gottstein and T. Al-Samman: *Mater. Sci. Forum*, 2005, vols. 495–497, pp. 623–32.
41. Y.N. Wang and J.C. Huang: *Mater. Chem. Phys.*, 2003, vol. 81, pp. 11–26.
42. D. Sarker and D.L. Chen: *Mater. Sci. Eng. A*, 2013, vol. 582, pp. 63–7.
43. T. Al-Samman and G. Gottstein: *Mater. Sci. Eng. A*, 2008, vol. 488, pp. 406–414.
44. I. Ulacia, S. Yi, M.T. Perez-Prado, N.V. Dudamell, F. Galvez, D. Letzig, and I. Hurtado: *Proc. 4th Inter. Conf. on High Speed forming*, Columbus, OH, 2010, March 9–10, pp. 189–97.
45. K.U. Kainer: *Proc. 7th Inter. Conf. on Magnesium Alloys and Their Application*, Dresden, Germany, 2006, November 6–9, pp. 161–63.
46. X. Li, F. Jiao, T. Al-Samman, and S.G. Chowdhury: *Scripta Mater.*, 2012, vol. 66, pp. 159–62.
47. X. Li, T. Al-Samman, S. Mu, G. Gottstein: *Mater. Sci. Eng. A*, 2012, vol. 528, pp. 7915–25.
48. J. Hirsch and T. Al-Samman: *Acta Mater.*, 2013, vol. 61, pp. 818–43.
49. A. Couret and D. Caillard: *Acta Metall.*, 1985, vol. 33, pp. 1447–54.
50. L. Helis, K. Okayasu, and H. Fukutomi: *Mater. Sci. Eng. A*, 2006, vol. 430, pp. 98–103.
51. H.T. Jeong and T.K. Ha: *J. Mater. Process. Technol.*, 2007, vols. 187–188, pp. 559–61.
52. R.W. Fonda and K.E. Knipling: *Sci. Technol. Weld. Joining*, 2011, vol. 16, pp. 288–94.
53. H.W. Lee, T.S. Lui, and L.H. Chen: *J. Alloys Compd.*, 2009, vol. 475, pp. 139–44.
54. S.H.C. Park, Y.S. Sato, and H. Kokawa: *Scripta Mater.*, 2003, vol. 49, pp. 161–66.
55. V.K. Patel, S.D. Bhole, and D.L. Chen: *Mater. Sci. Eng. A*, 2013, vol. 569, pp. 78–85.
56. F.A. Mirza, D.L. Chen, D.J. Li, and X.Q. Zeng: *Mater. Sci. Eng. A*, 2013, vol. 575, pp. 65–73.
57. F.A. Mirza, D.L. Chen, D.J. Li, and X.Q. Zeng: *Mater. Des.*, 2013, vol. 46, pp. 411–18.
58. C.L. Fan, D.L. Chen, and A.A. Luo: *Mater. Sci. Eng. A*, 2009, vol. A519, pp. 38–45.
59. X.Z. Lin and D.L. Chen: *J. Mater. Eng. Perform.*, 2008, vol. 17, pp. 894–901.
60. E. Schmid: *Z. Electrochem.*, 1931, vol. 37, p. 447.
61. M.R. Barnett: *Mater. Sci. Eng. A*, 2007, vol. 464, pp. 8–16.
62. C. Yan, W. Ma, V. Burg, and M.W. Chen: *J. Mater. Sci.*, 2007, vol. 42, pp. 7702–07.
63. P. Cizek and M.R. Barnett: *Scripta Mater.*, 2006, vol. 55, pp. 915–18.
64. Z. Keshavarz and M.R. Barnett: *Scripta Mater.*, 2008, vol. 59, pp. 959–62.
65. F.A. Mirza and D.L. Chen: in *Aerospace Materials Handbook*, S. Zhang and D.L. Zhao, eds., CRC Press/Taylor & Francis Group, Boca Raton, FL, 2013, pp. 647–98.
66. Y.N. Wang and J.C. Huang: *Acta Mater.*, 2007, vol. 55, pp. 897–905.
67. X. Li, T. Al-Samman, S. Mu, and G. Gottstein: *Mater. Sci. Eng. A*, 2011, vol. 528, pp. 7915–925.
68. D. Sarker and D.L. Chen: *Mater. Sci. Eng. A*, 2014, vol. 596, pp. 134–144.